

5

REACTIVE INTERMEDIATE STRUCTURES: A CASE STUDY*

5.1 Introduction

The first application of our third-generation UED apparatus, UED-3¹ was a study of the structural dynamics in the elimination of iodine from 1,2-diodotetrafluoroethane ($C_2F_4I_2$) to form tetrafluoroethylene (C_2F_4) on the picosecond time scale, and the direct determination of the molecular structure of the short-lived C_2F_4I radical intermediate—we determined it to

* Adapted from Ihee, H.; Lobastov, V. A.; Gomez, U.; Goodson, B. M.; Srinivasan, R.; Ruan, C.-Y.; Zewail, A. H., *Science* **2001**, *291*, 458; Ihee, H.; Goodson, B. M.; Srinivasan, R.; Lobastov, V.; Zewail, A. H., *J. Phys. Chem. A* **2002**, *106*, 4087.

be classical, not bridged in nature. The relevant structures for this reaction are shown below in Scheme 5–1.

The elimination reaction of $C_2F_4I_2$ is a prototypical reaction in ultrafast spectroscopic studies of photoinitiated reactions.^{2,3} The consecutive (nonconcerted) nature of the C–I bond breakage was elucidated via picosecond photofragment spectroscopy.² Following UV excitation, a biexponential formation of atomic iodine was observed—with a prompt component (≤ 1 ps) and a much slower second component (~ 30 – 150 ps, depending on the total excitation energy)—indicating a two-step process with a weakly bound radical intermediate (C_2F_4I). The femtochemistry of $C_2F_4I_2$ was subsequently investigated using femtosecond kinetic-energy resolved time-of-flight (KETOF) mass spectrometry, permitting the state, velocity, and angular evolution of the relevant species to be resolved.³ Femtosecond UV excitation (at 277 nm) causes the rapid (≈ 200 fs) loss of the first iodine atom, the first C–I bond breakage, and the formation of the transient C_2F_4I radical intermediate—with the kinetic energy distributions of the fragments directly measured. The remaining internal energy, left to redistribute within the vibrational degrees of freedom of the C_2F_4I radicals, was enough to induce secondary C–I fragmentation in a majority of the hot intermediates—resulting in the loss of the second iodine atom and the formation of the tetrafluoroethylene product in ≈ 25 ps.

The chemistry of halogen elimination reactions is of general interest because products are usually formed under stereochemical control with respect to the final positions of the functional groups about the newly formed double bond.⁴⁻⁷ The origin of this well-known behavior has been hypothesized to lie in the geometry of the intermediate species of the reaction. For example, previous quantum chemical calculations⁸ have shown that CH_2BrCH_2 and CH_2ICH_2 radicals should form stable, symmetrically “bridged” structures, consistent with the Skell hypothesis for the origin of stereochemical control in such systems.^{9, 10} In a symmetrically bridged structure, the primary halide (i.e., I or Br) is shared equally between the two $-\text{CR}_2$ moieties, whereas in a “classical” structure the primary halide would reside predominantly on one $-\text{CR}_2$ moiety.¹⁰ A bridged structure would prevent rotation about the C–C bond, thereby maintaining the functional group positions in the final product. However, the substitution of hydrogens with highly electronegative fluorines can cause dramatic changes in molecular structure (and reactivity). For example, it is well known that the CF_3 radical is highly non-planar while CH_3 is planar, and the $\text{C}_2\text{F}_4\text{I}$ radical structure may be much different from that of $\text{C}_2\text{H}_4\text{I}$.

While the presence of CF_2XCF_2 radicals can be readily detected in photodissociation reactions of $\text{CF}_2\text{XCF}_2\text{X}$ molecules via spectroscopy, UED offers the means to track all of the nuclear coordinates over the course of a

chemical reaction, allowing the molecular structures of these radicals to be observed directly. Thus, the elimination reaction of $C_2F_4I_2$ is an ideal process to study with UED: (1) it affords the opportunity to observe the structural dynamics of a prototypical non-concerted reaction involving the loss of two highly-scattering heavy atoms (providing a strong diffraction difference signal), and (2) it permits the determination of the molecular structure of a transient radical intermediate that belongs to an important family of chemical reactions.

5.2 Experimental

Samples of $C_2F_4I_2$ (Lancaster, 98%) were used without further purification, but were degassed with several freeze–pump–thaw cycles and stabilized with copper filings. High-purity xenon (Spectra Gases, 99.999%) was used as an atomic reference gas (see discussion below), and the CF_3I gas (99%) used for determining the zero-of-time in the lensing experiments was purchased from Aldrich. In order to maintain satisfactory sample pressure at the needle (estimated to be a few torr), the sample bulb, gas manifold, and nozzle temperatures were respectively maintained at 60 °C, 100 °C, and 120 °C for the $C_2F_4I_2$ experiments. The background pressure of the scattering chamber was typically $\sim 2 \times 10^{-4}$ torr during the experiment.

5.3 Results and Discussion

A. Ground-State Structures of C₂F₄I₂. The experimental results concerning the ground-state structures of C₂F₄I₂ are shown in Figs. 5–1 and 5–2. In order to observe the ground-state structures, we time the electron pulse to arrive before the initiation pulse (i.e., at a negative time). The C₂F₄I₂ molecule is known to have two conformational minima with respect to torsional rotation about the C–C bond: an *anti* structure with a \angle ICCI torsion angle of 180° and C_{2h} symmetry, and a *gauche* structure with \angle ICCI \approx 70° and C₂ symmetry. In the study by Hedberg and co-workers,¹¹ the experimental structural parameters for C₂F₄I₂ were refined under the simplifying assumption that the *anti* and *gauche* conformers possess identical values for the structural parameters, except for the \angle ICCI dihedral angle. Correspondingly, identical *anti/gauche* parameter values were used in our analysis, although recent quantum chemical calculations have suggested that the C–C and C–F distances of the *anti* conformers may be slightly shorter, and the C–I distances slightly longer, than those of the *gauche* conformers.¹²

Both ground-state structures were observed in the electron diffraction data shown in Fig. 5–1; the ratio of these conformers was determined via least-squares refinement to be 76:24 \pm 2 *anti:gauche*. This ratio, which is governed by the sample temperature and the energy difference between the

conformers, was identical to the previous results obtained by Hedberg and co-workers at 120 °C.¹¹ The theoretical $sM^T(-95\text{ ps}; s)$ curve, obtained from the refinement of the conformer ratio, is shown as the red curve in Fig. 5–2. Excellent agreement can be seen between $sM^E(-95\text{ ps}; s)$ and $sM^T(-95\text{ ps}; s)$, and in the corresponding experimental and theoretical $f(-95\text{ ps}; r)$ curves shown in Fig. 5–2.

The various interatomic distances present in the anti and gauche $\text{C}_2\text{F}_4\text{I}_2$ structures are indicated at the bottom of the $f(r)$ curve in Fig. 5–2 and can be summarized as follows: the peak at $\sim 1.4\text{ \AA}$ results from covalent C–F and C–C distances; the peak at $\sim 2.2\text{ \AA}$ results from covalent C–I and non-bonded F··F and C··F distances; the broad peak at $\sim 3\text{ \AA}$ is comprised of non-bonded F··I, C··I, and F··F distances; and the peaks at $\sim 3.8\text{ \AA}$ and $\sim 5.1\text{ \AA}$ respectively correspond to the non-bonded I··I distances for the gauche and anti conformers.

B. Structural Dynamics of the $\text{C}_2\text{F}_4\text{I}_2$ Reaction. UED images were acquired for the elimination reaction of $\text{C}_2\text{F}_4\text{I}_2$ over a range of time delays (t) from -95 ps to $+405\text{ ps}$. The data at -95 ps served as a reference representing the signal contributed only by parent molecules. A set of diffraction-difference curves with $t_{\text{ref}} = -95\text{ ps}$ was obtained from the images (see Fig. 5–3) using the procedures described in Chapter 4. Figure 5–4(a) shows the effects of the

Fourier filter on a raw diffraction-difference curve, $\Delta R^E(405 \text{ ps}; -95 \text{ ps}; s)$, while Fig. 5–5(a) shows the entire set of difference curves, $\Delta R^E(t; -95 \text{ ps}; s)$, and the corresponding residual background curves, $\Delta R_B^E(t; -95 \text{ ps}; s)$. No change is observed in the $t = -45 \text{ ps}$ data as the electron pulses probe the molecules prior to the initiation of the chemical reaction. At $t = 0 \text{ ps}$, a periodic pattern instantaneously appears (within our time resolution), resulting from structural changes in the molecules. The difference signal becomes more pronounced with increasing time.

The corresponding $\Delta sM^E(t; -95 \text{ ps}; s)$ curves, created in part by subtraction of the baseline curves obtained for each time delay, are shown in Fig. 5–5(b). The difference procedure removes most of the systematic background signal, resulting in a small, nearly linear background curve for the raw difference curves in Fig. 5–5(a). Finally, the corresponding time-dependent difference radial distribution curves, $\Delta f^E(t; -95 \text{ ps}; r)$, which directly indicate the structural changes occurring over the course of the reaction, are shown in Fig. 5–5(c). It is significant to note that the negative peak intensity at $\sim 5.1 \text{ \AA}$ in the $\Delta f(r)$ curves remains constant after 5 ps , whereas the peak intensities around $2\sim 3 \text{ \AA}$ continue to increase over a longer time scale.

As shown in the figure, the negative peak at $\sim 5.1 \text{ \AA}$ results from the

loss of the I·I internuclear separation of the anti conformer of the parent C₂F₄I₂ molecules, while those at 2~3 Å result primarily from the depletion of C-I, F·I, and C·I distances. These observations demonstrate the non-concerted nature of the structural changes in the reaction: the first step (C₂F₄I₂ → C₂F₄I + I) is essentially complete within our ~5 ps resolution—consistent with the ~200 fs time constant measured previously in this laboratory,³ whereas the second step (C₂F₄I → C₂F₄ + I) is considerably slower, taking place over tens of picoseconds.

Theoretical $\Delta sM^T(t; -95 \text{ ps}; s)$ and $\Delta f^T(t; -95 \text{ ps}; s)$ curves (red curves in Figs. 5-5(b) and 5-5(c)) were obtained by refining the relative fractions of the species present against the corresponding experimental $\Delta sM^E(t; -95 \text{ ps}; s)$ curve (blue) at each time delay. These refinements were performed as follows. The depletion of the C₂F₄I₂ parent molecules was fit using the structural parameters determined by Hedberg and co-workers, and with the anti:gauche conformer ratio held fixed at the 74:26 value determined above; the latter practice assumes that there is no disproportional selectivity in the depletion of anti *vs.* gauche C₂F₄I₂ conformers during the loss of the first iodine atom (i.e., that the C-I chromophores of the anti and gauche conformers have identical absorption cross sections and reactivity).

Starting structures for the C₂F₄I radical intermediate were constructed

using the structural parameters provided by recent quantum chemical calculations.⁸ While one goal of our studies was to experimentally determine the structure of this transient species, the calculations suggested that the structure of this species is non-bridged in nature, with anti and gauche conformers qualitatively similar to the parent structures. Nevertheless, we initially included a bridged C₂F₄I structure in our early fraction refinements; doing so, however, had a detrimental effect on the overall fits—and typically resulted in negative values for the bridged fraction. Therefore, our final fraction refinements of the $\Delta sM(t; -95 \text{ ps}; s)$ data included only the non-bridged, “classical” anti and gauche C₂F₄I structures.

The high internal energy of the C₂F₄I radical following laser excitation was included in our analysis. After each parent molecule absorbs a UV photon (107 kcal/mol) and fragments into C₂F₄I + I, 48 kcal/mol are available for the internal energy of the C₂F₄I radical and the translational motion of both fragments (for the I channel, whereas only 26 kcal/mol is left over after the formation of I*, spin excited iodine); 59 kcal/mol of the incident energy is required to break the first C–I bond (in addition to the 22 kcal/mol needed to match the spin-orbit energy of I*). According to previous experiments from this group,³ about 67% (for the I channel; 59% for I* channel) of the energy is partitioned into the translational degrees of freedom, whereas the remaining 33% [for the I channel (16 kcal/mol); 41% for the I* channel (11 kcal/mol)]

goes into the internal energy of the C_2F_4I radical. Accounting for the branching ratio of 30:70 for the I and I* channels³ yields 12.5 kcal/mol for the available internal energy acquired in the C_2F_4I radical. However, because some of the available thermal energy from the parent molecule at 393 K (~6.7 kcal/mol) remains in C_2F_4I , the total available internal energy is about 19 kcal/mol. If complete thermalization of the internal degrees of freedom is assumed, a vibrational temperature of ~800 K can be estimated for the C_2F_4I radical (based on the total remaining internal energy and quantum chemical predictions for the vibrational frequencies¹²). While the use of thermalized structures proved adequate for the present study, we note that in general, complete thermalization may not always be a good approximation—particularly for UED studies of complex molecules at high internal energies.¹³

Using theoretical values for the rotational barrier separating anti and gauche structures,¹³ microcanonical RRKM rates were calculated to predict the time constant for the conversion from the anti conformer to the gauche conformer to be ~13 ps, and that for the reverse isomerization to be ~3 ps. These time constants yield a steady-state anti:gauche conformer ratio of ~83:17. On the other hand, assuming complete thermalization of the internal degrees of freedom gives a similar conformer ratio of 81:19, estimated from the energy difference between the conformers (calculated to be ~3.3 kcal/mol¹²), and the internal temperature. In our refinements of the UED

data, the anti:gauche conformer ratio of the C₂F₄I radicals was therefore held fixed at 81:19. Note that the quantum chemical calculations predicted that the conformational energy difference between anti and gauche radicals is larger than the corresponding value for the parent conformers (~1.2–1.9 kcal/mol).¹² This larger energy difference apparently results from a relative stabilization of the anti radicals that has been rationalized in terms of hyperconjugation between the radical center and the σ*(C–I) molecular orbital.¹⁴

Finally, the structural parameters for the C₂F₄ product species were obtained from Ref. ¹⁵. The fraction refinements were thus simplified to a two-parameter fit: (1) the total fraction of C₂F₄I₂ parent molecules depleted, and (2) the total fraction of C₂F₄I radicals formed. The fraction of C₂F₄ product formed could then be determined from these values at each time point according to Eqn. 5–1:

$$\begin{aligned} \Delta sM(t; -95 \text{ ps}; s) = & -|\Delta p_{C_2F_4I_2}| \cdot sM(s)_{C_2F_4I_2} + |\Delta p_{C_2F_4I}| \cdot sM(s)_{C_2F_4I} \\ & + |\Delta p_{C_2F_4}| \cdot sM(s)_{C_2F_4} \end{aligned} \quad (5-1)$$

with

$$\Delta p_{C_2F_4} + \Delta p_{C_2F_4I} = -\Delta p_{C_2F_4I_2} \quad (5-2)$$

The time evolution of the distribution of structures is determined from

the $\Delta sM(t; -95 \text{ ps}; s)$ data. An initial depletion of the parental signal is observed to follow the response function of the UED apparatus, a result that is consistent with the ~ 200 fs time constant measured previously by femtosecond mass spectrometry.³ The amplitude of the diffraction-difference signals, when scaled to that of the ground state, shows that $\sim 8\%$ of the parent molecules participated in the reaction under the given experimental conditions. The relative fraction of $\text{C}_2\text{F}_4\text{I}$ rises briefly (within the response time of the apparatus) and then decays, while the fraction of C_2F_4 rises steadily. Fitting these time-dependent fractions results in an average time constant of 26 ± 7 ps for the depletion of $\text{C}_2\text{F}_4\text{I}$ transient structures (20 ± 5 ps) and formation of C_2F_4 molecules (31 ± 4 ps); the overall temporal resolution of the apparatus was explicitly included in the determination of these time constants. Given the available internal energy of the $\text{C}_2\text{F}_4\text{I}$ intermediate described above, this temporal behavior is entirely consistent with a barrier crossing process, as is the percentage of $\text{C}_2\text{F}_4\text{I}$ radicals undergoing further dissociation to form C_2F_4 ($55 \pm 5\%$).

C. Structural Change, Intermediate to Product: The $\text{C}_2\text{F}_4\text{I} \rightarrow \text{C}_2\text{F}_4 + \text{I}$ Process. As shown in the previous section, any reaction involving the parent molecules is complete within the first 5 ps. Thus, in order to highlight the structural changes of the reaction intermediate and product

only—with no contribution from any other species present—we generated a set of additional diffraction-difference curves with $t_{\text{ref}} = 5$ ps. Figure 5–6(a) shows raw difference curves [$\Delta R^E(t; 5 \text{ ps}; s)$] and the corresponding residual background curves [$\Delta R_B^E(t; 5 \text{ ps}; s)$]. The $\Delta sM^E(t; 5 \text{ ps}; s)$ curves, created in part by subtracting the baseline curves obtained for each time point, are shown in Fig. 5–6(b). As before, this difference procedure removes most of the background signal.

Figure 5–6(c) shows the corresponding difference radial distribution curves, $\Delta f^E(t; 5 \text{ ps}; r)$. The $\Delta f(t; 5 \text{ ps}; r)$ signals arise only from the transient $\text{C}_2\text{F}_4\text{I}$ and final product C_2F_4 species, with the depletion of the $\text{C}_2\text{F}_4\text{I}$ radical being evident at C–I, C·I, and F·I separations; note that the populations of other internuclear separations (e.g. C–F, C–C, and F·F) are essentially unchanged and make no contribution to the $\Delta sM^E(t; 5 \text{ ps}; s)$ or $\Delta f^E(t; 5 \text{ ps}; r)$ signals. The absence of an I·I component ($\sim 5.1 \text{ \AA}$) in the $\Delta f^E(t; 5 \text{ ps}; r)$ curves clearly shows that we are observing solely the population change of the transient $\text{C}_2\text{F}_4\text{I}$ structures forming C_2F_4 , and that the contribution from the unreacted $\text{C}_2\text{F}_4\text{I}_2$ population is negligible. Theoretical $\Delta sM^T(t; 5 \text{ ps}; s)$ and $\Delta f^T(t; 5 \text{ ps}; s)$ curves (red curves in Figs. 5–6(b) and 5–6(c)) were obtained by a single-parameter fit (the fraction of C_2F_4 species) of the experimental $\Delta sM^E(t; 5 \text{ ps}; s)$ curves according to Eqn. 5–3:

$$\Delta sM(t; 5 \text{ ps}; s) = -|\Delta p_{C_2F_4I}| \cdot sM(s)_{C_2F_4I} + |\Delta p_{C_2F_4}| \cdot sM(s)_{C_2F_4} \quad (5-3)$$

with

$$\Delta p_{C_2F_4} = -\Delta p_{C_2F_4I} \quad (5-4)$$

The time-dependent fraction of C_2F_4 formed after 5 ps, shown in Fig. 5-7, yields a time constant of 25 ± 7 ps, in total agreement with the above analysis of the $\Delta f(t; -95 \text{ ps}; r)$ curves.

D. Structure of the C_2F_4I Radical Intermediate. The molecular structure of the C_2F_4I radical intermediate was determined from the diffraction-difference curves $\Delta sM(t; 5 \text{ ps}; s)$; both bridged and classical C_2F_4I structures were considered in the fitting of the diffraction data. The symmetrically bridged structure has C_{2v} symmetry, whereas the *anti* and *gauche* conformers of the classical structure have C_s and C_1 symmetry, respectively. The $\Delta R^E(t; 5 \text{ ps}; s)$ difference curves from $t = +40$ ps to +405 ps were averaged (prior to Fourier filtering) to improve the precision of the fits. No significant changes in the structure of the radical are expected (or were observed) over this temporal range, as the internal energy of the radical should already be nearly equilibrated, and collisional cooling should not become important until well into the nanosecond regime under the present experimental conditions.

Prior to performing the time-averaged structural refinement for the $\text{C}_2\text{F}_4\text{I}$ radical, preliminary structural refinements were performed at each point in time in order to detect the presence of time-dependent structural changes within the $\text{C}_2\text{F}_4\text{I}$ species—manifested as far-from-equilibrium geometries¹³ in the early stages of the reaction. Most of the structural parameters showed little sign of temporal dependence, but the results for a few of the parameters were less conclusive. The C–I bond distance and $\angle\text{CCI}$ bond angle showed the greatest evidence for time-dependent changes at early time points (not shown), but further investigation is necessary before a definitive conclusion can be made; future UED studies with improved sensitivity, resolution, and analysis should be better able to determine the significance of far-from-equilibrium geometries in this reaction.

The signal, denoted $\Delta R^E(\infty; 5 \text{ ps}; s)$, was fit separately with starting structural parameters predicted from calculations for either the bridged species, or the 81:19 mixture of the classical (*anti* and *gauche*) species (the $\Delta R^E(\infty; 5 \text{ ps}; s)$ curve, along with the background curve obtained by fitting through the theoretical zero-crossing points, is shown in Fig. 5–4(c)). The results of this fitting procedure are contained in Fig. 5–8, where the experimental $\Delta sM^E(\infty; 5 \text{ ps}; s)$ and $\Delta f^E(\infty; 5 \text{ ps}; r)$ curves are shown along with the corresponding theoretical curves produced with the quantum chemical structures. As shown in Fig. 5–8, the theoretical curves for the mixture of

classical structures reproduce the experimental data extremely well, whereas the fit provided by the theoretical bridged structure is vastly inferior. Indeed, the $\Delta sM^E(\infty; 5 \text{ ps}; s)$ and $\Delta sM^T(\infty; 5 \text{ ps}; s)$ curves for the bridged structure in Fig. 5–8 clearly go out of phase, yielding manifestly different positions for the two prominent negative peaks in the corresponding $\Delta f^E(\infty; 5 \text{ ps}; r)$ and $\Delta f^T(\infty; 5 \text{ ps}; r)$ curves. Thus, we conclude that the structure of the $\text{C}_2\text{F}_4\text{I}$ radical intermediate is in fact classical in nature,¹ in general agreement with previous qualitative analysis from second-generation (UED-2) experiments.¹⁶

Significant improvements in sensitivity and resolution provided by the UED-3 apparatus permitted quantitative determination of the molecular structure of the $\text{C}_2\text{F}_4\text{I}$ radical from our experimental data, thereby allowing a direct comparison with quantum chemical calculations. A least-squares refinement of the $\Delta sM^E(\infty; 5 \text{ ps}; s)$ data was performed as follows. Reasonable assumptions were made to simplify the fit and reduce the number of adjustable parameters in the final structural refinement, as described below. Assuming a torsion angle of 180° , the *anti* conformer of the $\text{C}_2\text{F}_4\text{I}$ radical has 9 independent parameters—four covalent bond distances and five bond angles—when the structure is constrained to be geometrically consistent. The remaining (dependent) internuclear separations were obtained via trigonometric relations constructed in terms of the chosen independent parameters. The *gauche* conformer was treated similarly: it was described by

the same 9 independent parameters, but with values differing from those of the *anti* conformers by small constant amounts, as predicted by quantum chemical calculations.¹² For example, the calculations suggested that the C–I distance of the *gauche* conformer [$r(\text{C–I})_{gauche}$] would be less than that of the *anti* conformer by 0.015 Å; thus, $r(\text{C–I})_{gauche}$ was obtained by subtracting 0.015 Å from the refined value of $r(\text{C–I})_{anti}$. Again, following theoretical predictions, the primary dihedral angle of the *gauche* species was fixed at 56° as the dihedral angle was relatively insensitive in the fitting, partially due to the low amount of *gauche* structures present.

As before, the *anti:gauche* radical conformer ratio was held fixed at 81:19. The values for the mean amplitudes of vibration (l) and centrifugal distortion corrections (dr) for each atom–atom pair were calculated using the ASYM40 program developed by Hedberg and co-workers¹⁷ (assuming a thermal distribution of the internal energy within the C₂F₄I radical). These values were then entered into the structural refinement of the (geometrically consistent) internuclear distances (at the potential minima, r_e) and the bond angles using the relation $r_a \approx r_e + (3/2)al^2 + dr - l^2/r$, where r_a is the internuclear distance as measured by electron diffraction and a is the anharmonicity constant for the bond. The independent structural parameters obtained from the least-squares fit of the experimental data could then be compared to quantum chemical calculations.

The results of the least-squares structural refinement are shown in Fig. 5–9, and the values determined for the independent structural parameters are summarized in Table 5–1. The $r_e(\text{C–I})$ and $r_e(\text{C–C})$ distances of the $\text{C}_2\text{F}_4\text{I}$ radical are, respectively, longer and shorter than those of the parent molecule (for $\text{C}_2\text{F}_4\text{I}_2$, $r_e(\text{C–I}) \approx 2.136 \text{ \AA}$, $r_e(\text{C–C}) \approx 1.534 \text{ \AA}$),¹¹ while the $\text{C–F}'$ internuclear distance in the radical site ($-\text{CF}'_2$) is shorter than that of the $-\text{CF}_2\text{I}$ site. Moreover, the $\angle\text{CCF}'$ and $\angle\text{F}'\text{CF}'$ angles become larger than the corresponding angles of the parent (by $\sim 9^\circ$ and $\sim 12^\circ$, respectively¹¹), suggesting that the radical center ($-\text{CF}'_2$) of the $\text{C}_2\text{F}_4\text{I}$ intermediate relaxes following loss of the first I atom (naturally, a similar comparison may be drawn between these $\angle\text{CCF}'$ and $\angle\text{F}'\text{CF}'$ angles and the $\angle\text{CCF}$ and $\angle\text{FCF}$ angles on the other side of the radical). These results are consistent with the increased C–C bond order expected from the formation of the transient $\text{C}_2\text{F}_4\text{I}$ structure (Fig. 5–10). These trends were also well-reproduced by the quantum chemical calculations; indeed, the refined internuclear distances reported in Table 5–1 agree with the corresponding theoretical predictions to within 0.03 \AA .¹²

It is interesting to compare the molecular structure of the $\text{C}_2\text{F}_4\text{I}$ radical with that of the $\text{C}_2\text{H}_4\text{I}$ radical, and to consider the stereochemical implications for these intermediate species. However, while the geometry of the $\text{C}_2\text{F}_4\text{I}$ radical has now been studied with UED,^{1, 16} to date only quantum

chemical investigations of the C_2H_4I radical geometry have been performed (the high thermal instability of the $C_2H_4I_2$ parent molecule makes this substance notoriously difficult to work with in experimental studies). Quantum chemical structures of the C_2F_4I radical and the C_2H_4I radical, along with the corresponding energy contour maps, were calculated for both structures.^{8, 12} The energy contour maps, calculated using density functional theory (DFT) methods (B3PW91,^{18, 19} with the LAV3P basis set), were generated by optimizing the molecular geometry as a function of the position of the primary halogen atom (I); in both calculations, the position of the I atom was constrained to lie in the ICC plane bisecting the $\angle RCR$ angles (with $R=H$ or F). The dramatic difference between the C_2F_4I and C_2H_4I radical geometries in these calculations originated from the lower π electron density of the C_2F_4 moiety compared to that of the C_2H_4 moiety (due to electron withdrawal by the electronegative F atoms), which in turn affects the interaction between the p orbital of the primary halogen atom (I) and the π orbital of the $C-C$ bond in the bridged structure.

Recent theoretical investigations^{8,12} generalized this structural comparison to include a variety of CR_2XCR_2 -type radicals, where R represents either H or F , and X refers to the heavy halides (Cl , Br , and I). These calculations predicted that when $R=F$, then the most energetically stable radical structure is classical (with *anti* conformers always more stable

than *gauche* conformers); indeed, no minimum-energy structures with bridged geometries could be found for these species without at least one imaginary frequency (with the exception of CF_2ClCF_2 at the Hartree–Fock level). However, varying results were obtained with $\text{R}=\text{H}$: when $\text{X}=\text{I}$, then the most stable structure is predicted to be bridged; when $\text{X}=\text{Cl}$, the most stable structure is classical; and when $\text{X}=\text{Br}$, the result depends on the computational method used—B3PW91 DFT calculations using the LAV3P basis set predicted that the most stable structure would be bridged, but the same calculation using the LAV3P(d) basis set (which has an additional d orbital for the X atom) predicted a classical geometry for the global minimum (consistent with the results of a MRD-CI calculation performed elsewhere²⁰).

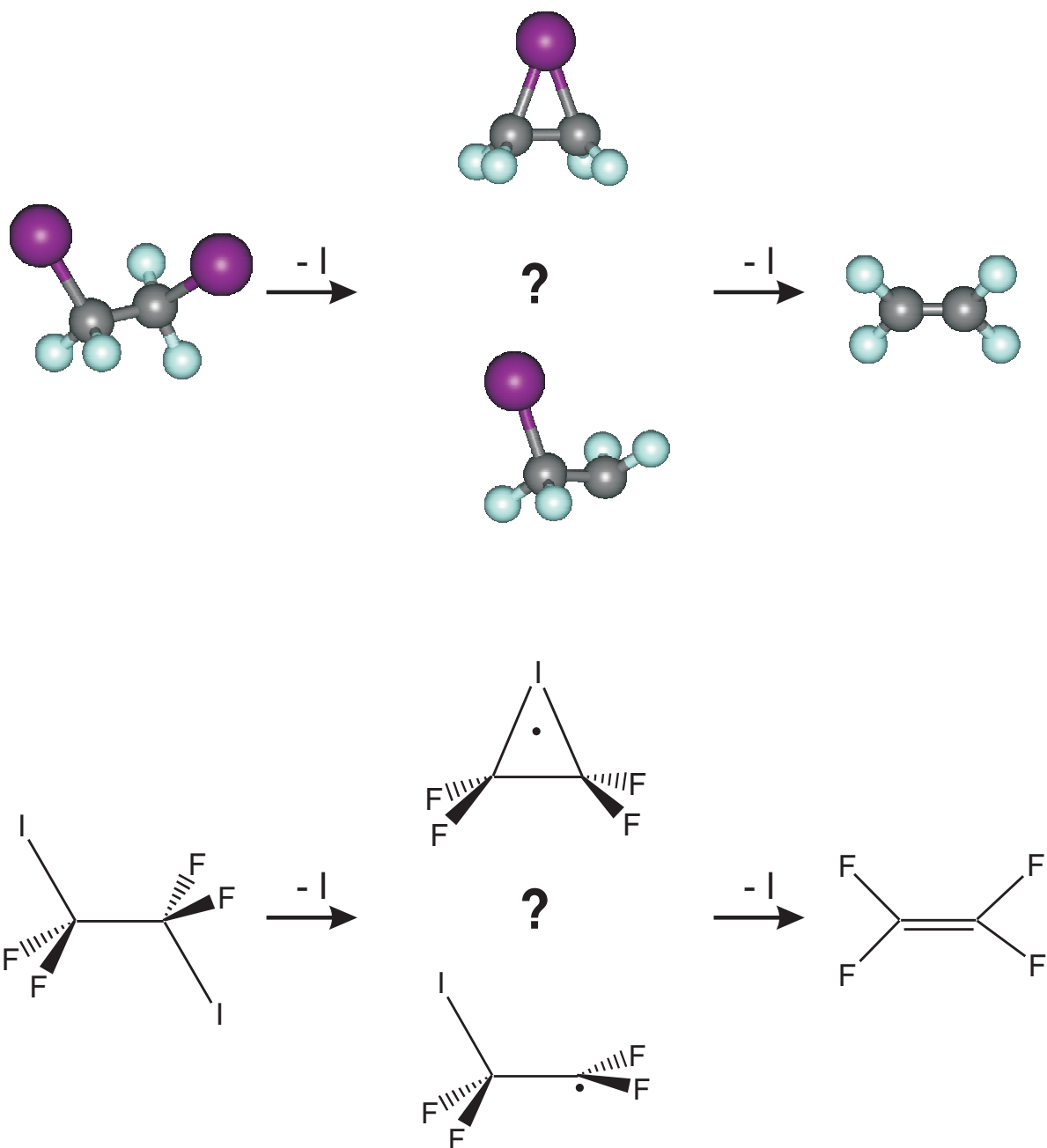
Much of the interest in the molecular structures of CR_2XCR_2 -type radicals lies in the relevance of structure and dynamics to the stereochemistry of reactions involving these transient species. For example, consider the generalized two-step elimination of 2X from $\text{C}_2\text{R}_4\text{X}_2$ giving C_2R_4 , shown schematically in Scheme 5–2. A number of $\text{C}_2\text{R}_4\text{X}$ intermediate structures could, in principle, be involved in the reaction, with different implications for the stereochemical control of the reaction with regard to the final positions of the $-\text{R}$ groups about the $\text{C}=\text{C}$ bond in the C_2R_4 product. The formation of a bridged $\text{C}_2\text{R}_4\text{X}$ structure prevents rotation about the $\text{C}-\text{C}$ bond, thereby ensuring stereochemical control in accordance with the Skell

hypothesis⁹ (a similar result would be obtained if the X atom were rapidly “shuttled” between the two $-\text{CR}_2$ moieties¹⁰). Alternatively, a classical structure could be formed, with either a “pyramidal” radical center (predicted for $\text{R}=\text{F}$ ¹²) or a nearly planar radical center (predicted for $\text{R}=\text{H}$ ¹²). Because rotation about the C–C bond is unhindered in classical structures, one might predict (contrapositively to the Skell hypothesis) that reactions involving $\text{C}_2\text{R}_4\text{X}$ radical intermediates that lack bridged geometries would *not* maintain stereochemical control (for nearly planar radical centers ($\text{R}=\text{H}$), the final positions of $-\text{R}_3$ and $-\text{R}_4$ could be scrambled through simple rotation about the C–C bond, whereas in species with $\text{R}=\text{F}$ the non-planar nature of the $-\text{CF}_2$ moiety might require some combination of rotation and inversion due to the high energy required to reach the “eclipsed” rotational transition state¹²).

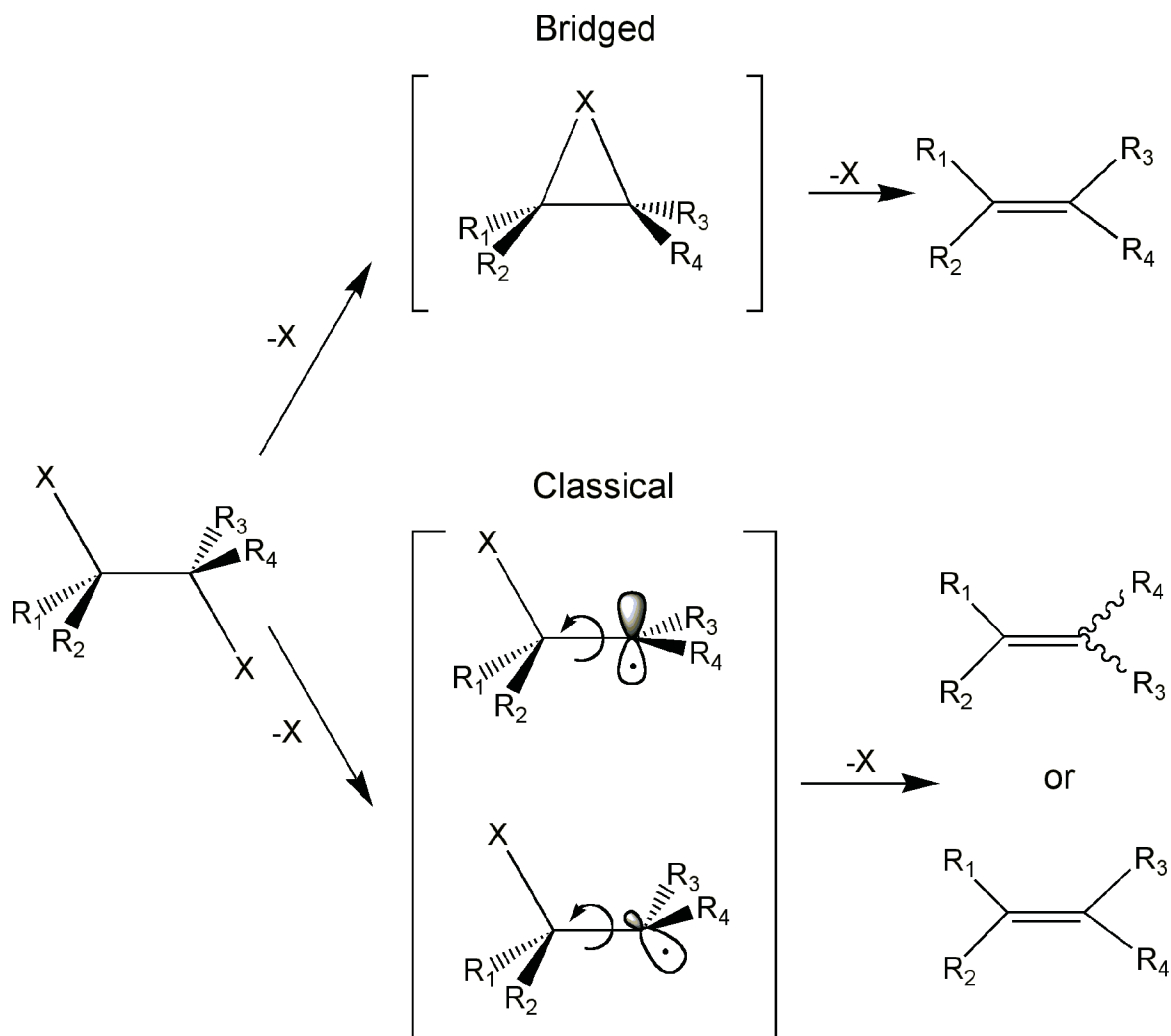
However, it should be considered that dynamical effects may also play a role in the retention of stereochemistry in such reactions; if the time for the second C–X bond breakage is shorter than that of rotation around the C–C bond, stereochemistry will be retained even in reactions involving classical $\text{C}_2\text{R}_4\text{X}$ structures. Future studies on other $\text{C}_2\text{R}_4\text{X}$ species may shine new light on the respective roles of structure and dynamics in determining the stereochemical nature of the products formed by various reactions.

5.4 Conclusions

In summary, significant improvements in instrumentation provided by our third generation apparatus now permit UED to study structural dynamics in chemical reactions with unprecedented temporal and spatial resolution. These experimental advances have been accompanied by improvements in data processing and use of the diffraction-difference analysis, which were described here in detail. These advances were borne out in the first application of the new apparatus—the study of the non-concerted elimination of iodine from $C_2F_4I_2$. The structural changes occurring over the course of the reaction were followed with temporal resolution of ~ 5 ps, with spatial resolution approaching 0.01 \AA , and with sensitivity to chemical change of $\sim 1\%$. The high sensitivity and spatiotemporal resolution permitted the molecular structure of the transient intermediate C_2F_4I to be determined and refined: the radical is classical, not bridged, in nature—in quantitative agreement with quantum chemical predictions to within 0.03 \AA . In the future, additional UED studies of other C_2R_4X intermediates and related species should provide considerable insight into the respective roles of structure and dynamics in stereochemical control.



Scheme 5-1. Non-concerted elimination reaction of $C_2F_4I_2$ with the hitherto unknown reaction intermediate.



Scheme 5-2. Schematic of dihalide elimination reactions involving C_2R_4X radical intermediates. Once the parent molecule $C_2R_4X_2$ loses the first X atom, the intermediate species C_2R_4X is formed. In the case of a bridged intermediate structure (top brackets), the retention of stereochemical selectivity is derived from the inhibition of rotation about the C-C bond (top product). However, in the case of the classical structure (bottom brackets), the situation is more complex. Rotation about the C-C bond is allowed; if the time scale for the elimination of the second -X atom is much faster than the rotation, one can expect stereochemical selectivity (bottom product), whereas stereochemical control would be lost if the situation were reversed (middle product). With regard to the geometry of the radical site in the classical structure, simple rotation about the C-C bond (prior to the loss of the second X atom) would suffice for the loss of stereochemical control for structures with planar radical centers (middle intermediate), whereas species with non-planar radical centers (bottom intermediate) may require a combination of rotation and inversion.

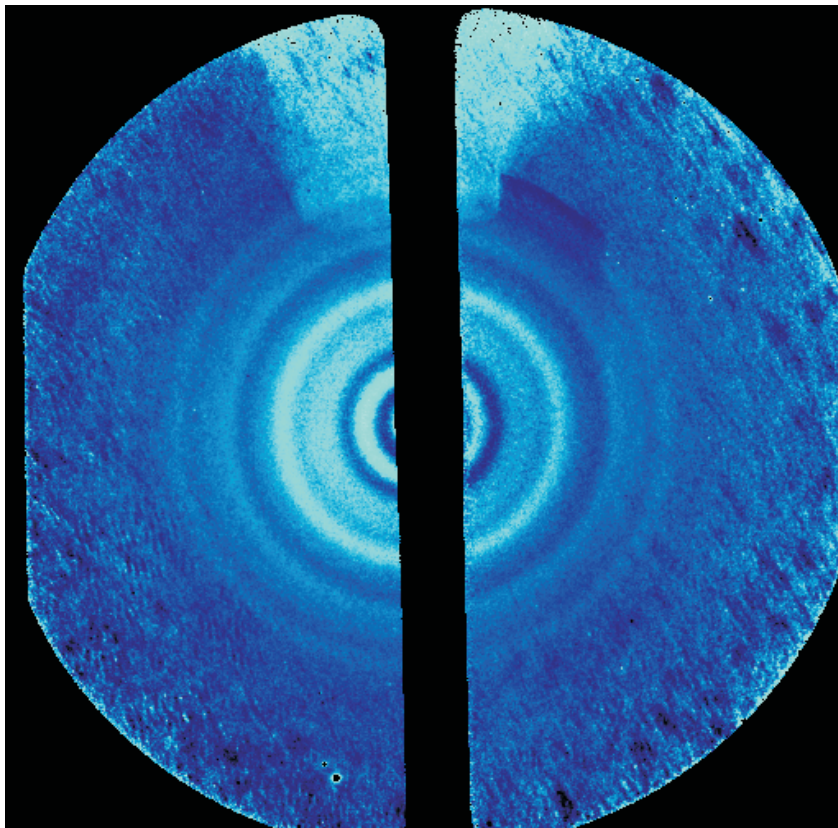


Figure 5-1. Ground-state molecular diffraction image of $C_2F_4I_2$.

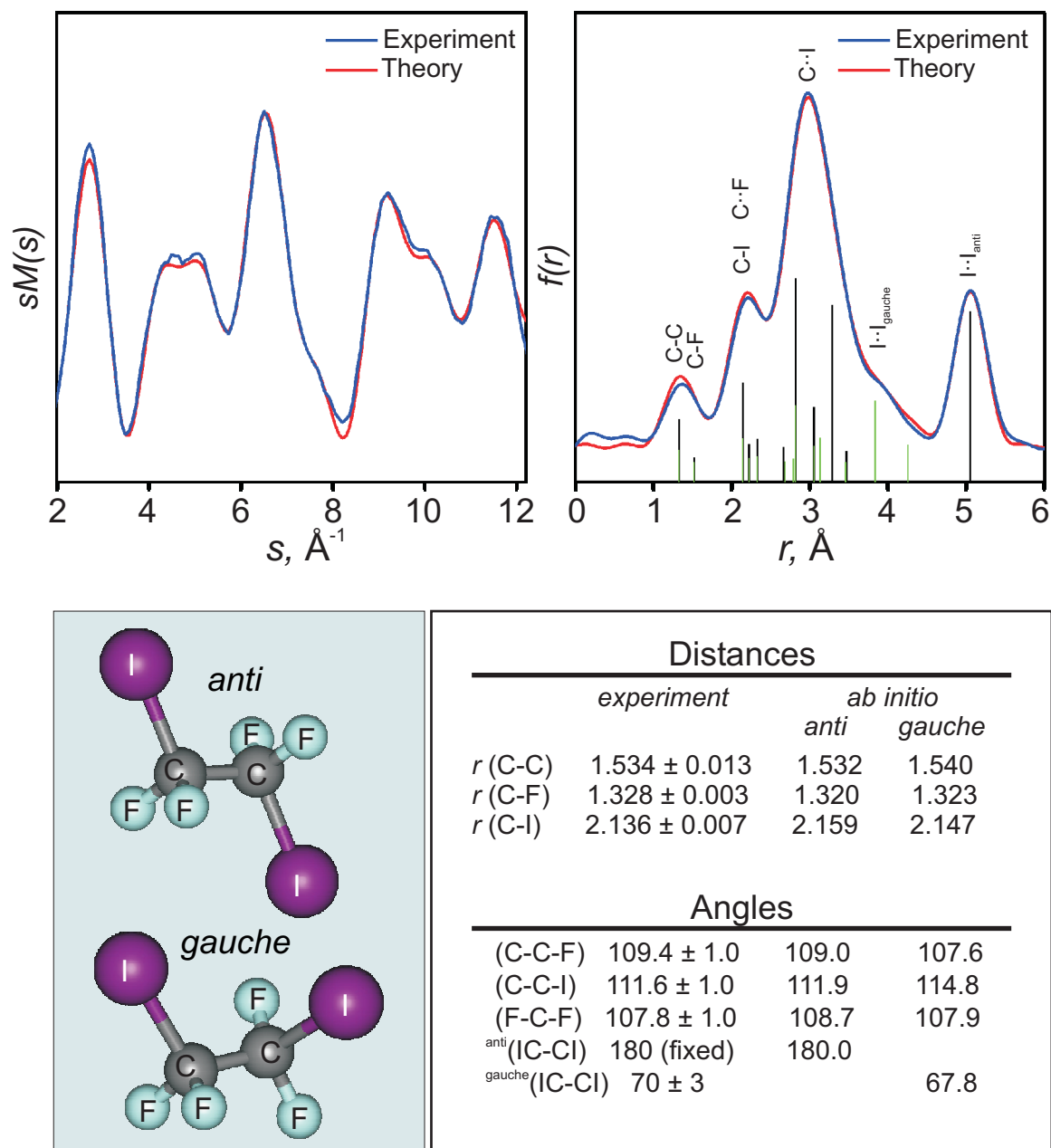
Molecular Structure of $C_2F_4I_2$ 

Figure 5-2. Refined ground-state structure of $C_2F_4I_2$. The comparison between the experimental and refined theoretical $sM(s)$ and $f(r)$ curves is shown, along with the determined bond distances and angles for the *anti* and *gauche* conformers. Distances are in ångströms, and angles are in degrees. The bond distances for the *anti* (black) and *gauche* (green) isomers are indicated by vertical lines at the bottom of the $f(r)$ panel.

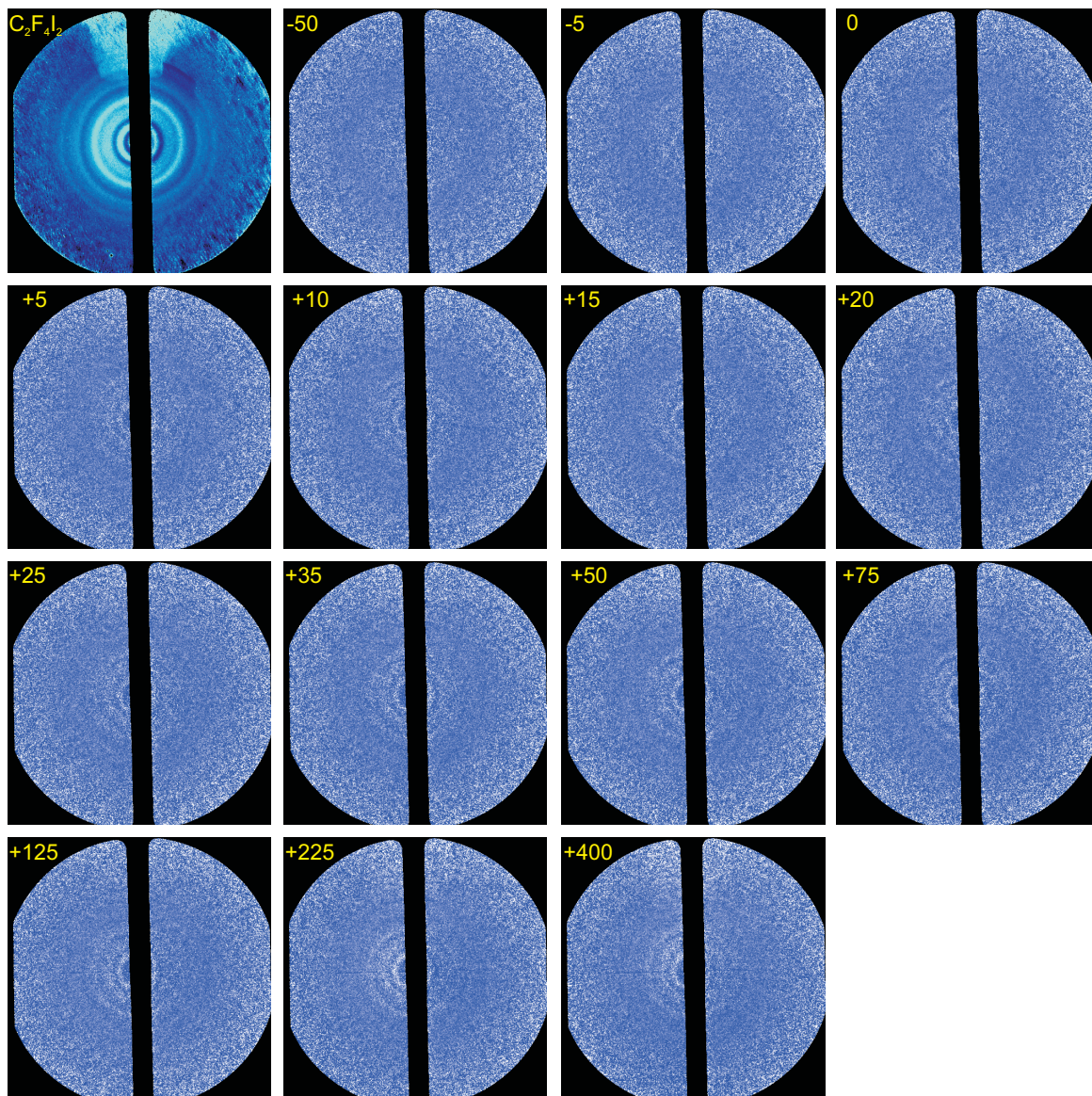


Figure 5-3. Time-resolved 2D diffraction-difference images of $C_2F_4I_2$ ($t_{\text{ref}} = -100$ ps). Each frame is identified by the relative time delay (in picoseconds) between the laser pump and electron probe pulses. The emergence of rings in the difference images with increasing time delay reflects the ensuing molecular structural dynamics. The first image is the ground-state image.

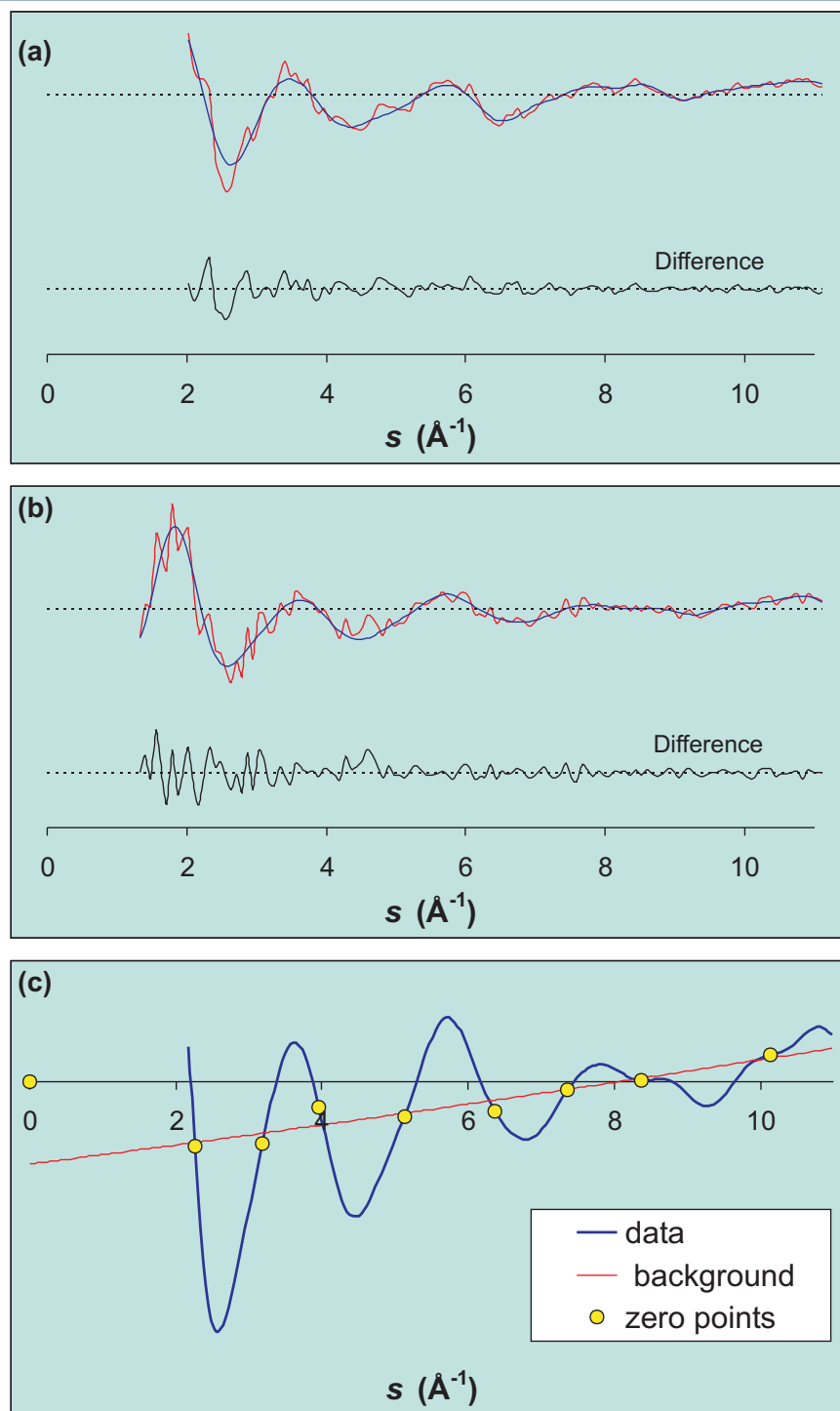


Figure 5-4. (a,b) The effect of Fourier filtering on 1-D raw diffraction-difference curves. The raw data is shown in red, and the Fourier filtered data (obtained with a 8.7-\AA low-pass filter) is shown in blue. The difference between the raw and filtered data shows the noise removed by the filter. (a) $R^E(405 \text{ ps}; -95 \text{ ps}; s)$. (b) $R^E(\infty \text{ ps}; 5 \text{ ps}; s)$. (c) Background fitting through the zero-crossing points of the experimental $R^E(\infty \text{ ps}; 5 \text{ ps}; s)$ data. The experimental $R^E(\infty \text{ ps}; 5 \text{ ps}; s)$ is shown in blue, and the background $R^E_B(\infty \text{ ps}; 5 \text{ ps}; s)$, obtained by fitting a low-order polynomial through the zero-crossing points (yellow circles), is shown in red.

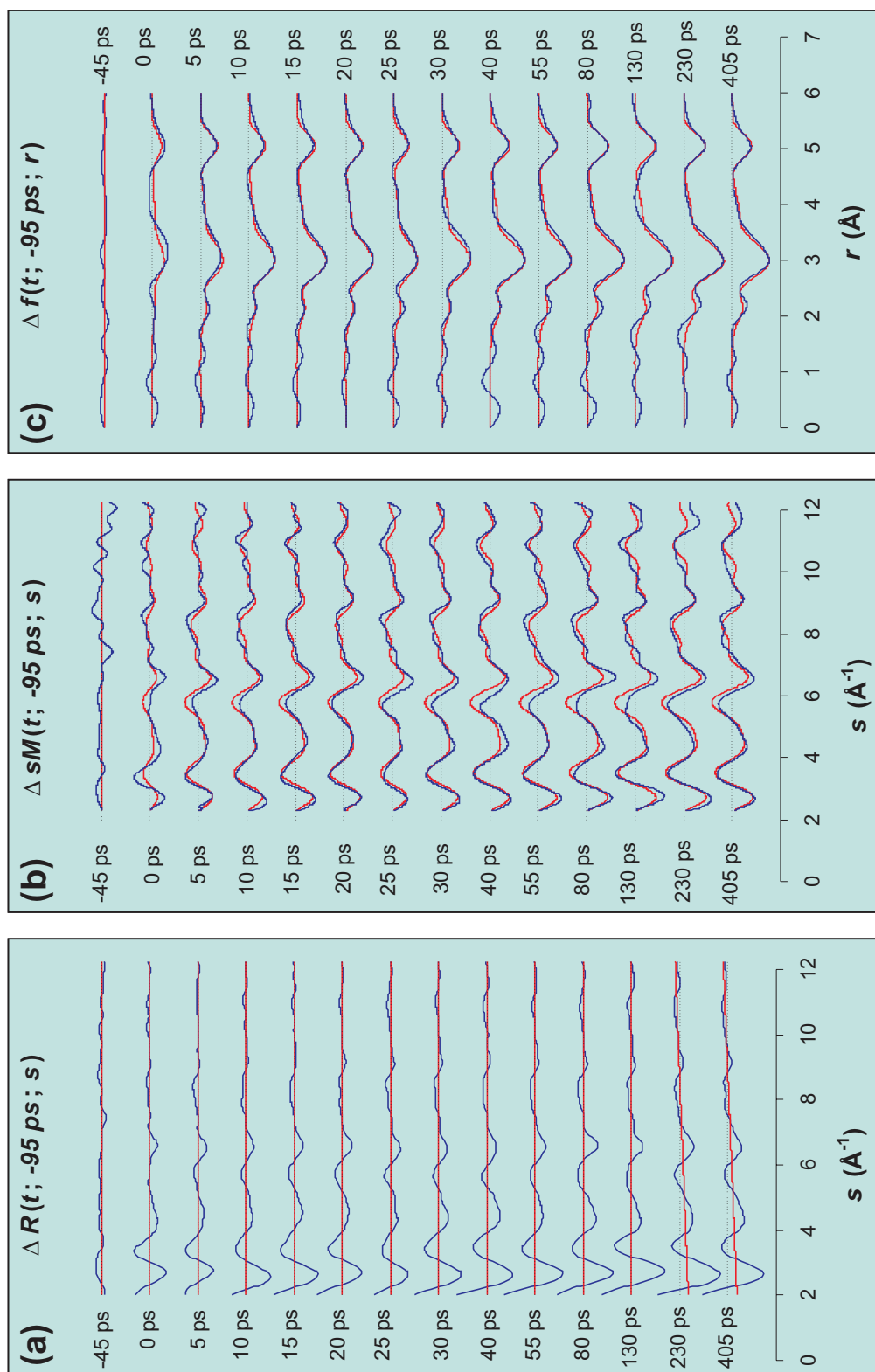


Figure 5-5. Time-resolved structural changes from the elimination of iodine from $\text{C}_2\text{F}_4\text{I}_2$. (a) Raw diffraction-difference signals, $R(t; -95 \text{ ps}; s)$, (blue curves), shown with the baseline curves (red). (b) Experimental (blue) and theoretical (red) $sM(t; -95 \text{ ps}; s)$ curves obtained at varying time delays. (c) Corresponding experimental (blue) and theoretical (red) $f(t; -95 \text{ ps}; r)$ curves. Major peaks are highlighted with arrows.

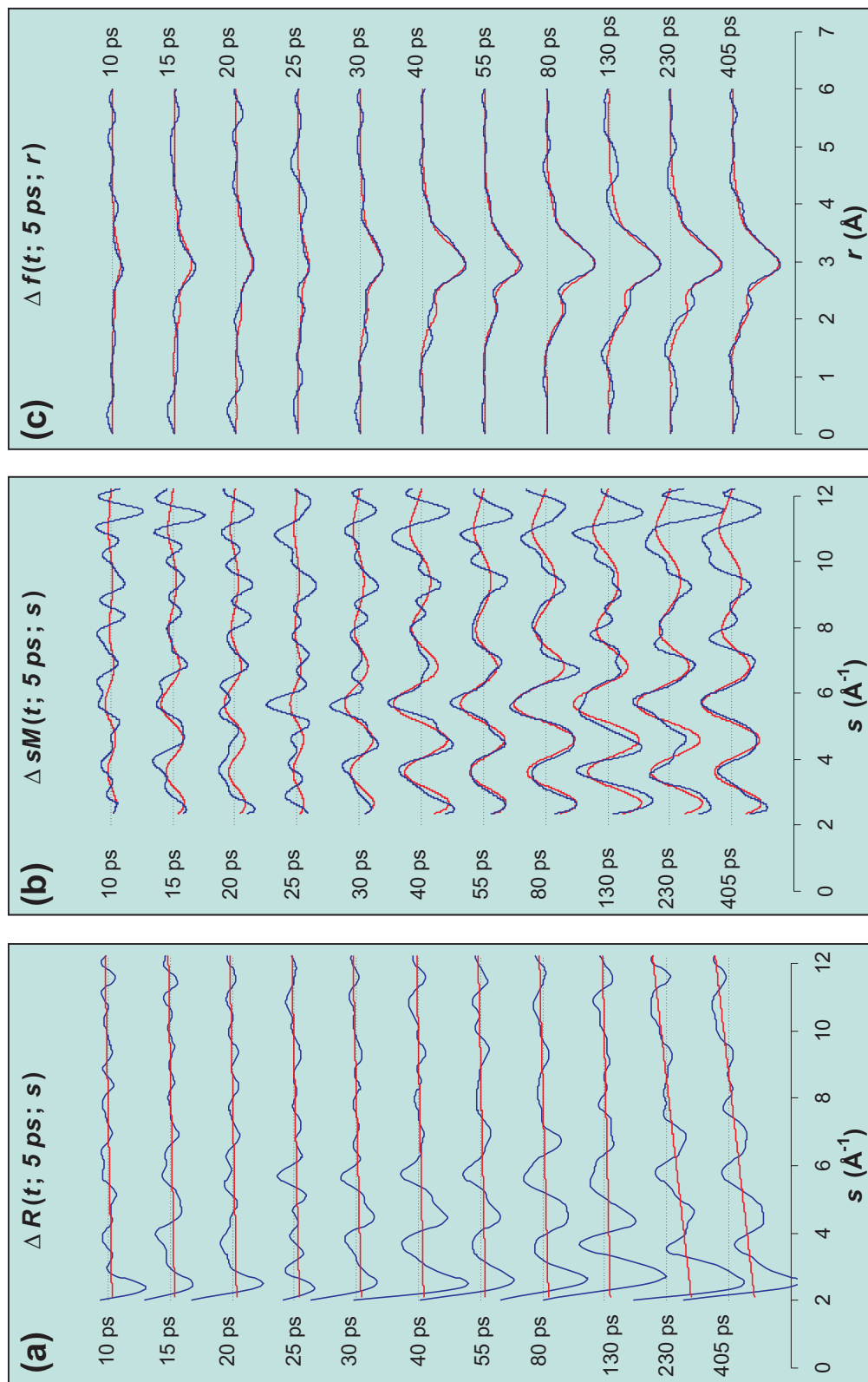


Figure 5-6. Time-resolved structural changes involving only the $\text{C}_2\text{F}_4\text{I}_2 \rightarrow \text{C}_2\text{F}_4 + \text{I}$ contribution to the diffraction-difference signal. (a) Raw diffraction-difference signals, $R(t; 5 \text{ ps}; s)$, (blue curves), shown with the (nearly linear) baseline curves (red). (b) Experimental (blue) and theoretical (red) $sM(t; 5 \text{ ps}; s)$ curves obtained at varying time delays. (c) Corresponding experimental (blue) and theoretical (red) $f(t; 5 \text{ ps}; r)$ curves. Note the absence of a peak at $\sim 5.1 \text{ \AA}$ corresponding to the depletion of $\text{I} \cdots \text{I}$ internuclear distances.

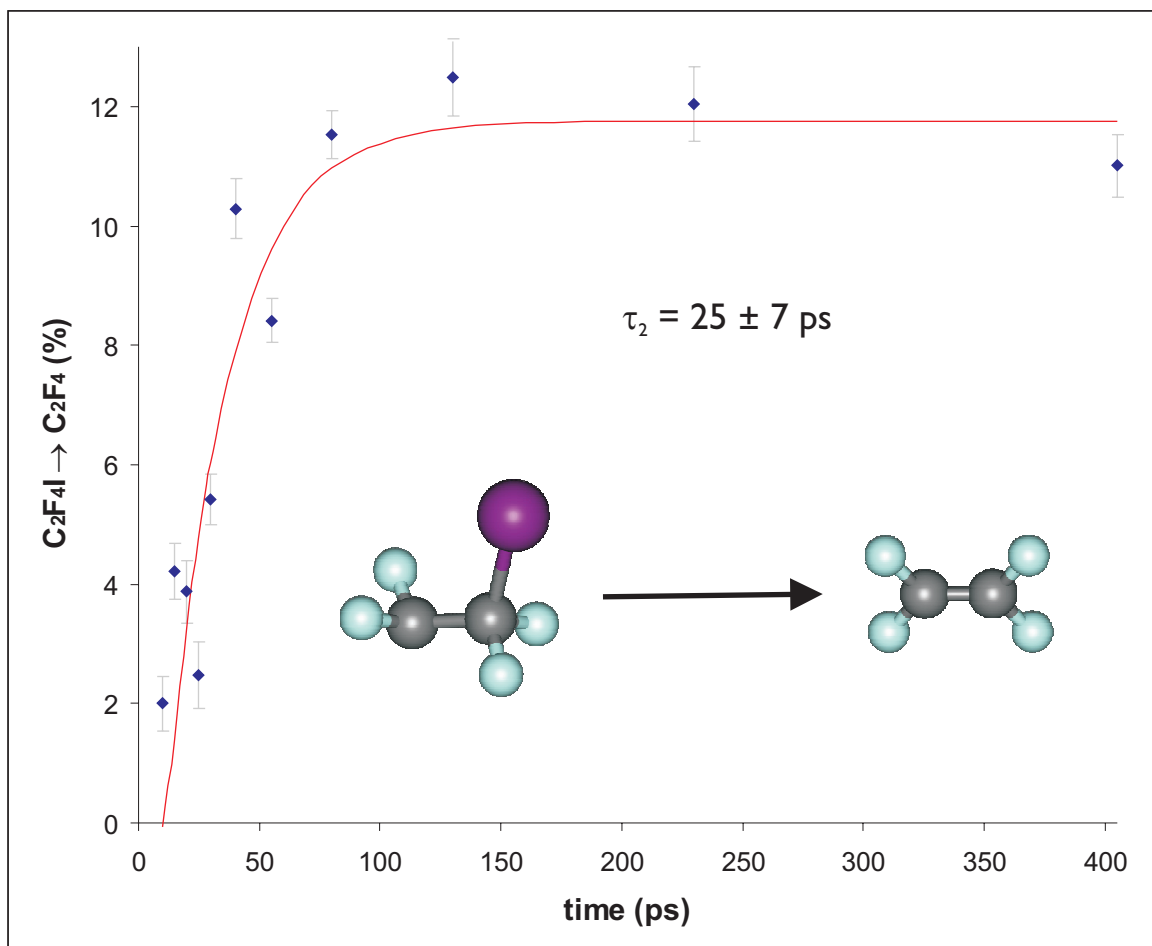


Figure 5-7. Time dependence of the formation of C_2F_4 molecules from the decay of C_2F_4I transient structures in the $sM(t; 5\text{ ps}; s)$ data. The curve is an exponential fit of the C_2F_4 fraction (with the temporal pulse widths of the electron and laser pulses taken into account); the apparent time constant for the formation of C_2F_4 was of 25 ± 7 ps. Each error bar represents one standard deviation.

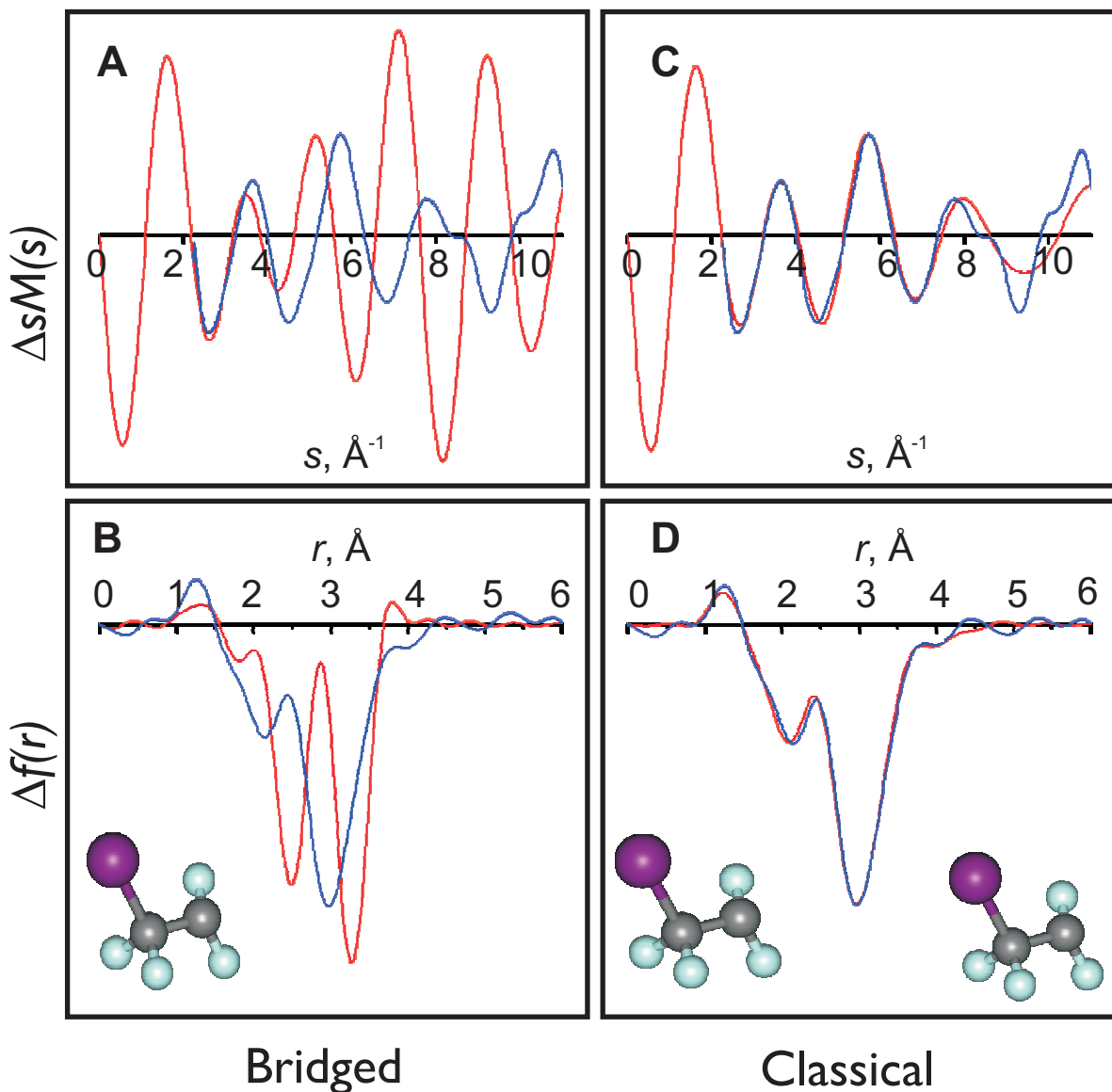
Structure of C_2F_4I Transient Intermediate

Figure 5-8. Structural determination of the transient C_2F_4I intermediate. **(A, B)** Comparison of experimental $sM(\infty; 5 \text{ ps}; s)$ and $f(\infty; 5 \text{ ps}; r)$ curves (blue) with corresponding theoretical curves (red) obtained via *ab initio* calculations of the bridged structure for C_2F_4I . **(C, D)** Comparison of experimental $sM(\infty; 5 \text{ ps}; s)$ and $f(\infty; 5 \text{ ps}; r)$ curves with theoretical curves obtained using the *ab initio* classical (*anti* and *gauche*) C_2F_4I structures.

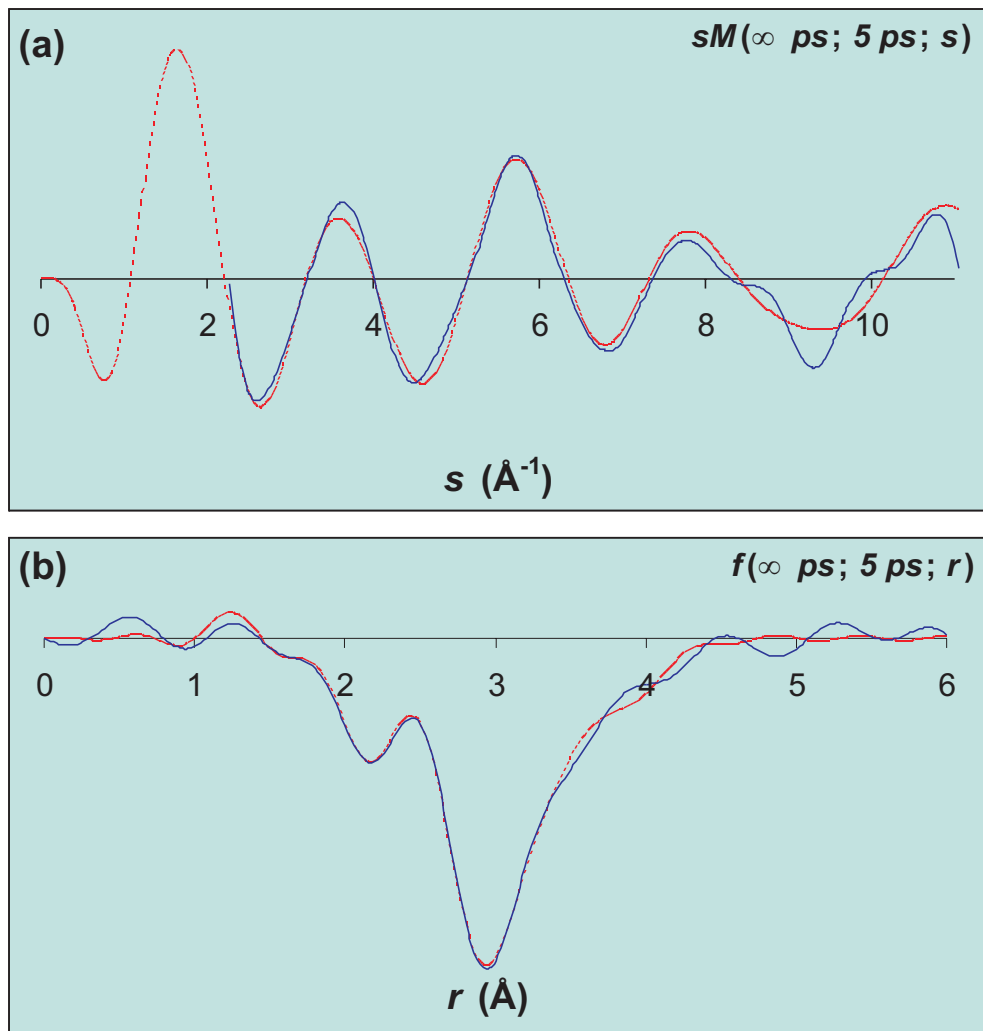


Figure 5-9. Refinement of the C_2F_4I radical structure. (a,b) Comparison of experimental $sM(5 \text{ ps}; s)$ (a) and $f(5 \text{ ps}; r)$ (b) curves (blue) with corresponding theoretical curves (red) obtained from the least-squares refinement of the C_2F_4I structure (see text).

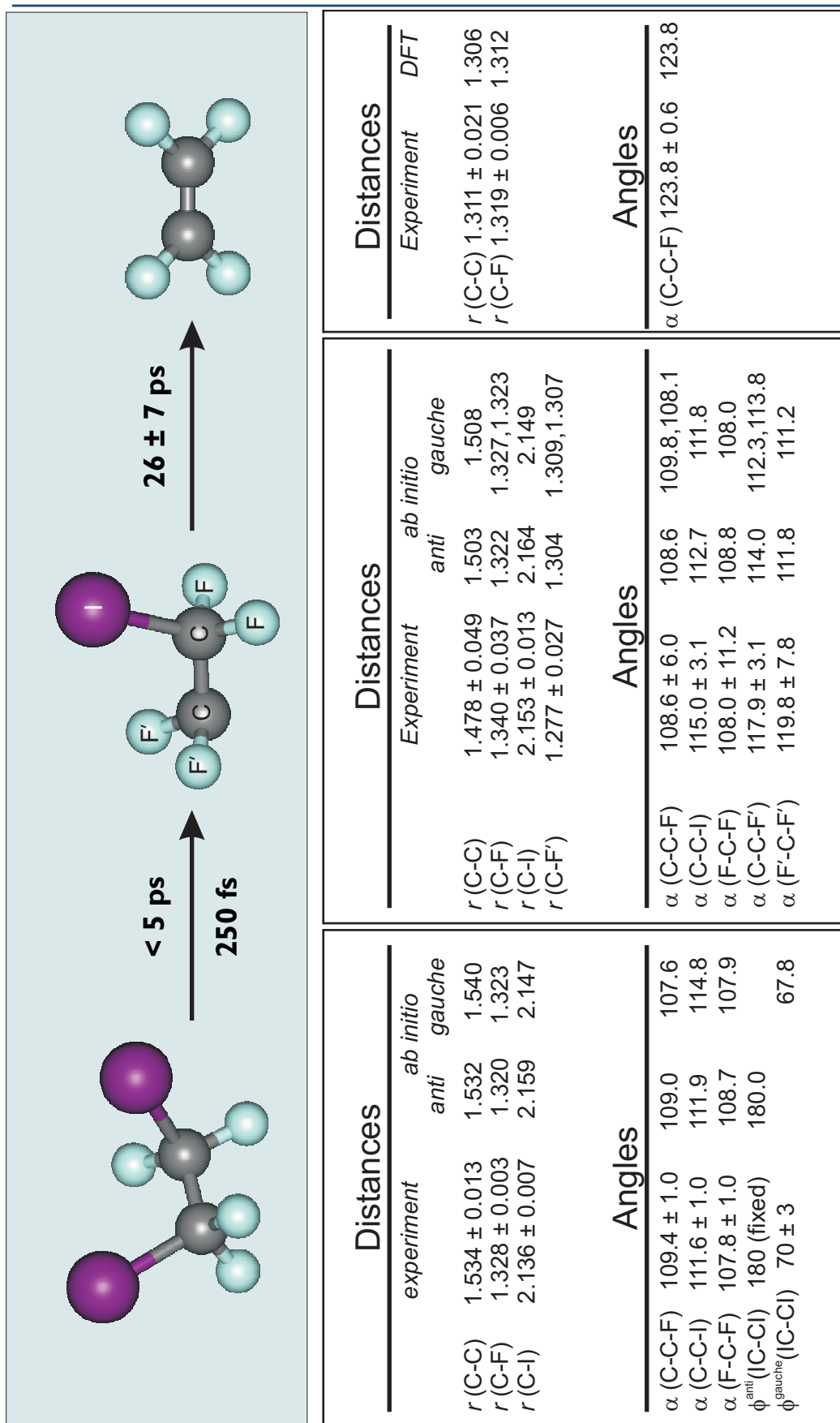
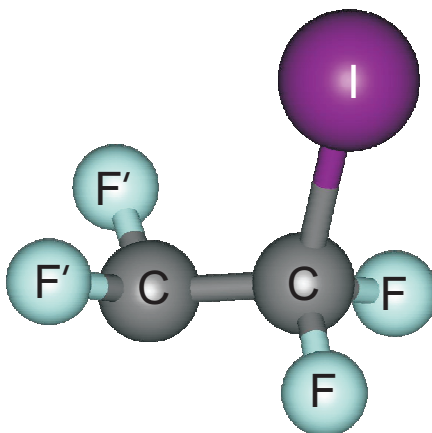


Figure 5-10. Complete structural determination of the $\text{C}_2\text{F}_4\text{I}_2$ elimination reaction. The bond distances and angles for all three species are shown, along with the DFT values for comparison. Distances are in ångströms, and angles are in degrees. Note that the C–C bond distance becomes progressively shorter from reactant through intermediate to product, thus reflecting the change in bond order from a single bond to a double bond. Also, note the change in bond angles of C_2F_4 which reflects relaxation of structure.



	Experiment	Predicted Values	
	<i>anti</i>	<i>anti</i>	<i>gauche</i>
$r(\text{C}=\text{C})$	1.478 ± 0.049	1.503	1.508
$r(\text{C}-\text{F})$	1.340 ± 0.037	1.322	1.327, 1.323
$r(\text{C}-\text{I})$	2.153 ± 0.013	2.164	2.149
$r(\text{C}-\text{F}')$	1.277 ± 0.027	1.304	1.309, 1.307
$\angle \text{CCI}$	115.0 ± 3.1	112.7	111.8
$\angle \text{CCF}$	108.6 ± 6.0	108.6	109.8, 108.1
$\angle \text{FCF}/2$	54.0 ± 5.6	54.4	54.0
$\angle \text{CCF}'$	117.9 ± 3.1	114.0	112.3, 113.8
$\angle \text{F}'\text{CF}'/2$	59.9 ± 3.9	55.9	55.6

Table 5-1. Comparison of the experimental values of the independent structural parameters of the classical $\text{C}_2\text{F}_4\text{I}$ radical intermediate with those obtained via quantum chemical calculations. The bond distances are in ångströms and the bond angles are in degrees.

References

1. Ihee, H.; Lobastov, V. A.; Gomez, U.; Goodson, B. M.; Srinivasan, R.; Ruan, C.-Y.; Zewail, A. H., *Science* **2001**, *291*, 458.
2. Khundkar, L. R.; Zewail, A. H., *J. Chem. Phys.* **1990**, *92*, 231.
3. Zhong, D.; Ahmad, S.; Zewail, A. H., *J. Am. Chem. Soc.* **1997**, *119*, 5978.
4. Kochi, J. K., *Free Radicals*. John Wiley & Sons: New York, 1973.
5. Beckwith, A. L. J.; Ingold, K. U., Free-Radical Rearrangements. In *Rearrangements in Ground and Excited States*, de Mayo, P., Ed. Academic Press: New York, 1980.
6. Kerr, J. A., *Handbook of Bimolecular and Termolecular Gas Reactions*. CRC Press: Boca Raton, 1981.
7. Fossey, J.; Lefort, D.; Sorba, J., *Free Radicals in Organic Chemistry*. John Wiley & Sons: New York, 1995.
8. Ihee, H.; Zewail, A. H.; Goddard III, W. A., *J. Phys. Chem. A* **1999**, *103*, 6638.
9. Skell, P. S.; Tuleen, D. L.; Radio, P. D., *J. Am. Chem. Soc.* **1963**, *85*, 2849.
10. Skell, P. S.; Traynham, J. G., *Acc. Chem. Res.* **1984**, *17*, 160.
11. Thomassen, H.; Samdal, S.; Hedberg, K., *J. Am. Chem. Soc.* **1992**, *114*, 2810.
12. Ihee, H.; Kua, J.; Goddard III, W. A.; Zewail, A. H., *J. Phys. Chem. A* **2001**, *105*, 3623.

-
13. Ruan, C. Y.; Lobastov, V. A.; Srinivasan, R.; Goodson, B. M.; Ihee, H.; Zewail, A. H., *Proc. Natl. Acad. Sci. USA* **2001**, *98*, 7117.
 14. Bernardi, F.; Bottoni, A.; Fossey, J.; Sorba, J., *J. Mol. Struct.* **1985**, *119*, 231.
 15. Carlos, J. L.; Karl, R. R. J.; Bauer, S. H., *J. Chem. Soc. Farad. Trans. II* **1973**, *70*, 177.
 16. Cao, J. M.; Ihee, H.; Zewail, A. H., *Proc. Natl. Acad. Sci. USA* **1999**, *96*, 338.
 17. Hedberg, L.; Mills, I. M., *J. Mol. Spectrosc.* **1993**, *160*, 117.
 18. Becke, A. D., *Phys. Rev. A* **1988**, *38*, 3098.
 19. Perdew, J. P.; Chevary, J. A.; Vosko, S. H.; Jackson, K. A.; Pederson, M. R.; Singh, D. J.; Fiolhais, C., *Phys. Rev. B* **1992**, *46*, 6671.
 20. Engels, B.; Peyerimhoff, S. D., *J. Mol. Struct.* **1986**, *138*, 59.